

## Evaluation of the seismic response of a homogeneous earth dam

S. Rampello<sup>a</sup>, E. Cascone<sup>b,\*</sup>, N. Grosso<sup>b,1</sup>

<sup>a</sup> Dipartimento di Ingegneria Strutturale e Geotecnica, Università di Roma La Sapienza, Italy

<sup>b</sup> Dipartimento di Ingegneria Civile, Facoltà di Ingegneria, Contrada di Dio, Università di Messina, 98166 Messina, Italy

### ARTICLE INFO

#### Article history:

Received 8 April 2008  
Received in revised form  
30 July 2008  
Accepted 19 August 2008

#### Keywords:

Earth dam  
Seismic response  
Effective stress analysis  
Displacement methods  
Decoupled approach

### ABSTRACT

The response of an earth dam to seismic loading is studied through displacement-based analyses and finite element, effective stress dynamic analyses. Displacement-based analyses are carried out using both empirical relationships and the decoupled approach in which the deformable response of the soil is accounted for through ground response analyses, and the resulting accelerograms are used in the sliding block analysis. The FE analyses are carried out using a constitutive model capable to reproduce soil non-linearity, calibrated against laboratory measurements of the stiffness at small strains. The influence of the assumed input motion and bedrock depth on the seismic response of the dam is also studied.

The FE analyses permitted evaluation of the overall patterns of the dam behaviour in terms of displacements and of stress, strain and acceleration fields. For any of the seismic scenarios considered in the analyses the performance of the dam was satisfactory in that maximum computed settlements at the crest were considerably smaller than the service freeboard of the dam and limited shear strains were obtained within the dam during earthquake loading. Comparison of FE dynamic analyses with displacement-based analyses allowed predictions from different approaches to be compared. A fair agreement was obtained provided that ground response analysis was accounted for when using the displacement-based approach.

© 2008 Elsevier Ltd. All rights reserved.

### 1. Introduction

Evaluation of stability conditions and crest displacements of earth dams is an issue of major concern in seismic regions. Seismic-induced deformations in an earth dam may lead to overtopping and consequently to severe losses in terms of property and human lives.

In recent years, a revision of seismic hazard maps and design criteria has led to the necessity of assessing the seismic safety of earth dams previously built without consideration of seismic-induced forces. As a consequence, design of proper remedial measures has become a challenging problem for geotechnical engineers.

The study of the seismic response of earth dams is a complex problem that generally requires the use of dynamic methods of analysis. These vary from highly simplified to rigorous methods, and consequently require different levels of sophistication in terms of proper problem formulation, characterisation of material properties and modelling of stress–strain soil behaviour.

Nowadays coupled effective stress dynamic analyses can be carried out using advanced constitutive models for soil behaviour

in which the soil is treated as a two-phase material with fully coupled soil skeleton response and excess pore water pressure development [1,2]. Inelastic soil behaviour under cyclic loading can be properly described through elastic–plastic constitutive models developed within the framework of bounding surface plasticity, kinematic hardening plasticity or generalised plasticity. Alternatively, non-linear soil behaviour can be modelled using given stress–strain relationships to represent the cyclic behaviour in simple shearing and empirical relationships to evaluate pore water pressure build-up under earthquake loading [3]. Advanced soil models can provide accurate predictions for static and dynamic loading conditions and have been used successfully in analyses of earth dams [4,5]. However, they often require parameters not usually measured in field or laboratory testing. Moreover, uncertainties are often related to seismic input when analysing real boundary value problems.

Due to the uncertainties mentioned above, the response of earth dams to earthquake loading is often evaluated through displacement-based approaches, decoupling the ground response analysis of the earth structure from the sliding block analysis [6–10].

In this paper, the response of a homogeneous earth dam under seismic loading was studied through both displacement-based analyses and FE effective stress dynamic analyses. The supplementary geotechnical investigation carried out at the site provided a reliable set of stiffness properties, allowing the shear

\* Corresponding author. Tel.: +39 090 397 7162; fax: +39 090 397 7480.

E-mail address: [cascone@ingegneria.unime.it](mailto:cascone@ingegneria.unime.it) (E. Cascone).

<sup>1</sup> Formerly post-doc student.

stiffness at small strains to be evaluated for the earth dam and the foundation soil. The effect of non-linear soil behaviour was then accounted for in both the displacement-based decoupled approach and in the FE analyses from the early beginning of earthquake loading.

Displacement-based analyses were carried out at different degrees of complexity. First, empirical relationships proposed in the literature [11–13] were applied. Then, sliding block analyses were carried out assuming a rigid-perfectly plastic soil behaviour. Finally the decoupled approach was applied carrying out 1D and 2D equivalent linear ground response analyses followed by sliding block analyses.

The FE analyses were carried out using an elastic-plastic soil model with isotropic hardening, capable to reproduce some features of cyclic soil behaviour. Model parameters were calibrated against consolidated undrained triaxial compression tests and resonant column tests.

Both real and artificial accelerograms were used as input motions and four different depths of the bedrock  $z_B$  were assumed in the range of 25–300 m. This permitted to evaluate the influence of factors such as bedrock depth, input motion and parameter calibration on the response of the dam to earthquake loading, gaining some insight in its behaviour under seismic conditions.

**2. Site description and input motion**

The dam is located in Southern Italy and dikes the course of the Marana Capacciotti stream. Fig. 1 shows a plan view of the dam and its main cross section; Table 1 summarises the main geometrical features of the dam. The drainage system consists of a sub-vertical central drain discharging into a tunnel parallel to the longitudinal axis of the dam and of a drain located at the toe of the downstream slope. An impervious diaphragm extending into the lower clay deposit prevents seepage through the alluvial soils underlying the dam. The figure shows the location of four extensometers installed at the crest and the downstream slope to monitor the settlement of the dam during the construction and after its completion for a period of about 10 years. Supplementary in situ investigation, recently carried out to assess the seismic performance of the dam, involved three boreholes (BH), four cone penetration tests (CPT) and laboratory tests on 21 undisturbed

tube samples for reliable evaluation of stiffness and strength properties of dam and foundation soils.

The foundation soil includes two layers: an alluvial soil deposit, about 12 m thick, made of medium-stiff silt and clay ( $I_L = 0.3$ ) of low plasticity ( $I_p = 13.5\%$ ) with thin layers of sand and gravel and a stiff silty clay deposit ( $I_L = 0.1$ ) of low plasticity ( $I_p = 16\%$ ), which extends down to the deep bedrock formation. The dam embankment is mainly formed by sandy silt and clay of low plasticity ( $I_p = 18.7\%$ ). A detailed description of the geotechnical characterisation of the site may be found in Calabresi et al. [14] and Cascone and Rampello [10].

Both artificial and real accelerograms were considered in the seismic analyses of the dam. A set of 10 artificial accelerograms were generated to match the response spectrum provided by the Eurocode no. 8 (EC8) for soil type A, that is for rock or rock-like formations with equivalent shear wave velocity, in the first 30 m,  $V_{S30} \geq 800$  m/s, and for earthquake magnitude  $M > 5.5$  [15]. The accelerograms are characterised by a wide frequency content, peak ground acceleration  $a_{max}$  of about 0.35g, duration of the event  $T_D = 30$  s and values of the Arias intensity ranging in the interval  $I_A = 3.5$ –4.7 m/s. The value of  $a_{max} = 0.35g$  is consistent with the results of a seismic hazard study that, for a return period of 475 years, predicts at the site peak ground accelerations of 0.28–0.32g [16]. The real accelerograms selected for the analyses are characterised by values of  $a_{max}$  in the range of 0.3–0.5g, and by plateau of the normalised response spectrum approximately similar to that given by EC8 for soil type A and  $M > 5.5$ . In the analyses, the peak ground acceleration of each of them was scaled to the same value of  $a_{max} = 0.35g$  adopted for the artificial accelerograms.

These two sets of accelerograms were initially used to perform a decoupled seismic analysis of the earth dam, in which the

**Table 1**  
Dam geometrical features

Volume	3.71 M m <sup>3</sup>
Water storage	49 M m <sup>3</sup>
Crest length	837 m
Crest width	7.5 m
Height	48 m
Freeboard	2.6 m
Slopes	1/2–1/5

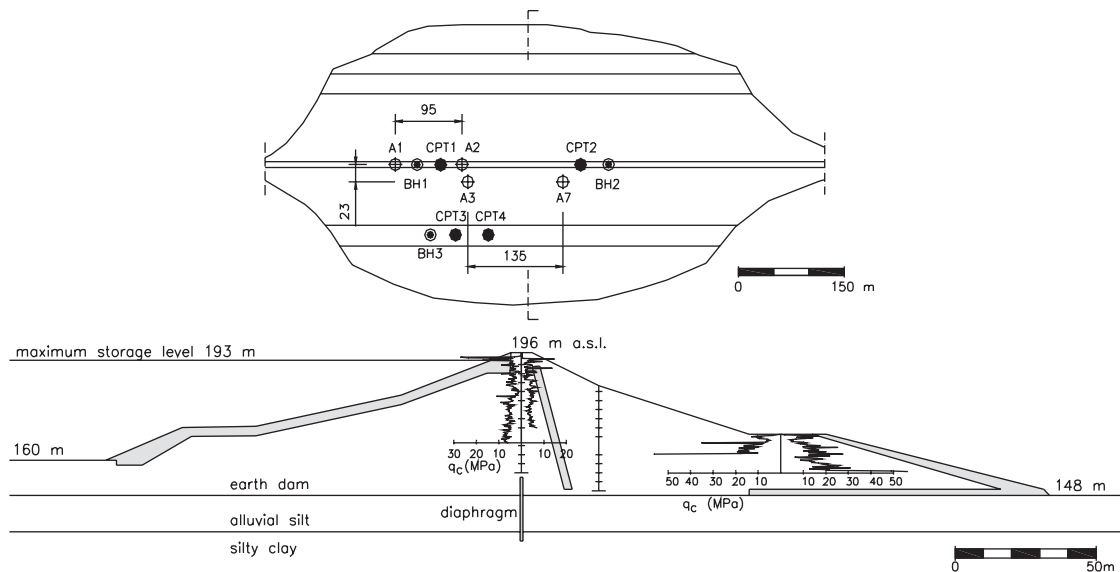


**Fig. 1.** Plan view and main cross section of Marana Capacciotti dam (adapted from [14]).

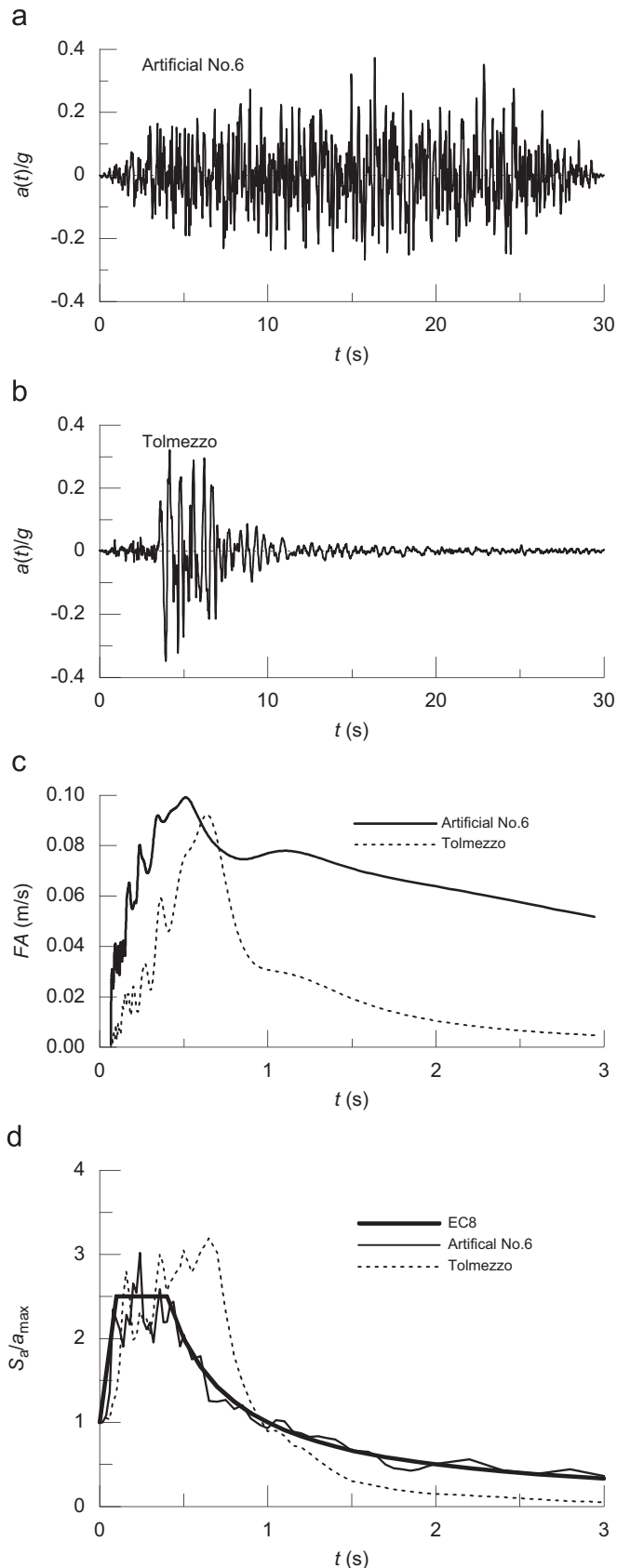


**Fig. 2.** Input accelerograms: (a) artificial accelerogram no. 6; (b) scaled Tolmezzo accelerogram; (c) Fourier amplitude spectra and (d) normalised response spectra.

dynamic response analysis of the earth structure was performed separately from the sliding block analysis. The ground response analyses were carried out under both 1D and 2D conditions, incorporating the non-linear soil behaviour through the equivalent linear method, and assuming four different depths for the bedrock. The accelerograms were assumed to be applied at the rock outcrop; analysis input motions were then obtained by 1D deconvolution of the outcropping accelerograms to each assumed bedrock depth. Sliding block analyses were then carried out to evaluate the dam displacements using the accelerograms obtained at the centre of gravity of the critical failure surfaces. Using this approach, the seismic performance of the dam was evaluated for a range of earthquake loadings, and the most critical seismic scenarios were detected [10].

In the FE effective stress seismic analyses described in the present study only the artificial accelerogram no. 6 and the accelerogram recorded at Tolmezzo during the 1976 Friuli earthquake were used. These accelerograms were in fact among those that yielded the largest displacements in the decoupled seismic analysis of the dam [10].

The artificial accelerogram no. 6, shown in Fig. 2a, is characterised by a significant duration of the strong motion phase; in fact, the bracketed duration, defined as the time between the first and last exceedances of a threshold acceleration, set equal to  $0.05g$ , is  $T_D \cong 27$  s. It has a large bandwidth (Fig. 2c), and an Arias intensity  $I_A = 3.96$  m/s. Fig. 2b shows the Tolmezzo accelerogram after scaling the peak ground acceleration ( $a_{\max} = 0.37g$ ) to the same value of  $a_{\max} = 0.35g$  adopted for the artificial accelerogram. The bracketed duration of the strong motion phase is of 6.2 s and the Arias intensity is  $I_A = 1.42$  m/s. The Fourier amplitude spectra and the normalised response spectra of the two accelerograms are compared in Fig. 2c–d. The spectrum of the artificial motion has the typical shape of a wide-band motion, whereas the spectrum of the scaled real motion is characterised by a well defined predominant period  $T_P = 0.68$  s. Fig. 2d shows that the spectral acceleration amplitudes of the artificial and the real accelerograms are comparable in the range of periods corresponding to the plateau of the EC8 spectrum for soil type A. However, values of spectral acceleration for the real motion are higher than those given by the EC8 spectrum for periods in the range of 0.5–1.0 s; the opposite is observed for  $T > 1.5$  s.

Geotechnical investigation did not encounter a soil layer stiff enough to be regarded as a bedrock ( $V_s > 800$  m/s). A geological study of the site provides an estimate of the bedrock depth of about 300 m. Therefore, a parametric study was performed, in which the influence of the bedrock depth on the dam response was evaluated. For this purpose, four different bedrock depths  $z_B$  were selected:  $z_B = 25, 50, 100$  and 300 m.

### 3. Displacement-based methods

#### 3.1. Simplified displacement methods

The simplest approach for evaluating the seismic performance of earth structures is represented by the displacement-based methods derived from the sliding block analysis [17]. According to this method the earthquake-induced displacement of the potential sliding mass is evaluated following a two-step procedure: first, the critical acceleration and the associated failure mechanism are determined via the pseudo-static approach; then, the cumulative displacement of the potential sliding mass is computed by double integration of the acceleration of the sliding soil mass relative to firm ground. This approach is the theoretical basis for a number of simplified methods proposed for evaluating the

**Table 2**  
Empirical relationships used for simplified displacement evaluation

Reference	Average displacement	Earthqs. no.	M	No. of accels.	Notes
[11]	$u = \frac{37v_{max}^2}{a_{max}} e^{-9.4(a_c/a_{max})}$	14	6.3–6.7	28	$a_{max} > 0.15g$
[12]	$\log u = 0.90 + \log \left[ \left( 1 - \frac{a_c}{a_{max}} \right)^{2.53} \left( \frac{a_c}{a_{max}} \right)^{-1.09} \right]$	11	6.6–7.2	50	$u$ (cm)
[13]	$\log u = 1.460 \log I_A - 6.642 \frac{a_c}{g} + 1.546$	7	5.8–7.5	11	$a_{max} > 0.13g$ $I_A = 0.2-9.96$ m/s, $u$ (cm)

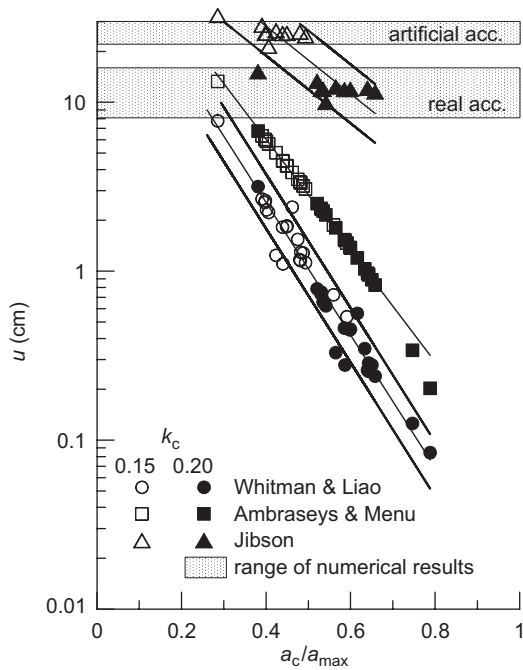


**Fig. 3.** Displacements computed using simplified methods.

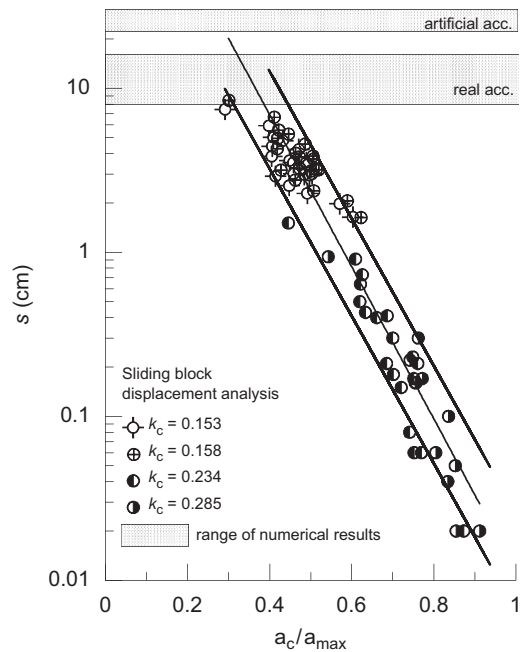


**Fig. 4.** Displacement at the dam crest evaluated using the sliding block method.

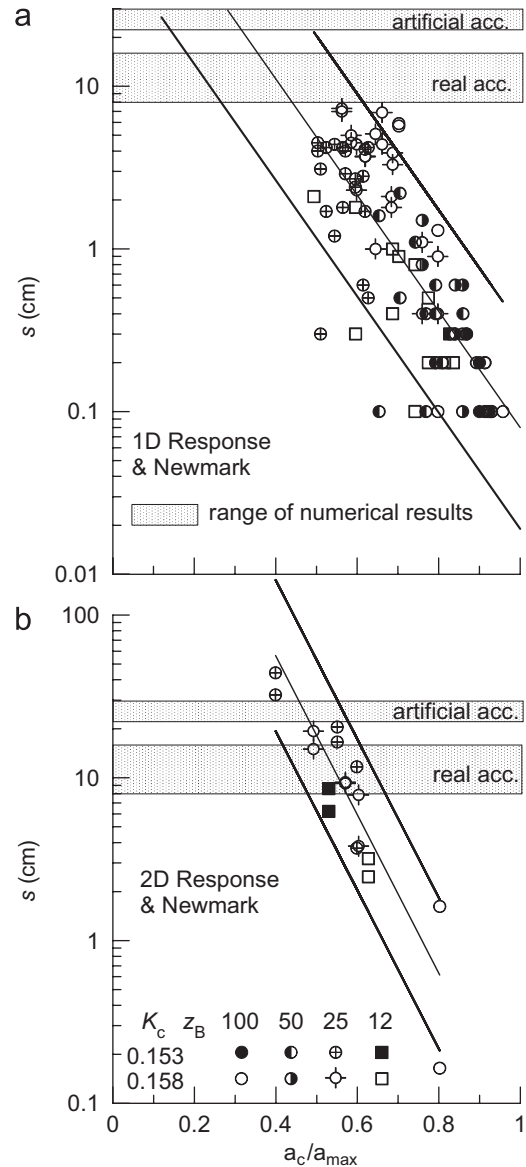


**Fig. 5.** Displacements at the dam crest computed via decoupled approaches: (a) 1D and (b) 2D ground response analyses.

earthquake-induced displacements of slopes, derived by fitting displacements computed for different values of the critical acceleration and for different sets of earthquake records. These simplified methods predict permanent displacement  $u$  as a function of the critical acceleration  $a_c$  and some parameters

related to seismic shaking, such as peak acceleration  $a_{max}$ , peak velocity  $v_{max}$  or Arias intensity  $I_A$ . A comprehensive review of the available simplified displacement methods may be found in Cai and Bathurst [18].

The methods used in this study to compute earth dam displacements were those proposed by Whitman and Liao [11], Ambraseys and Menu [12] and Jibson [13]. Table 2 reports the empirical relationships providing average values of displacement together with some details concerning the seismic motions considered in developing the equations. Only the artificial accelerograms were used in the computations.

Two values of the critical acceleration were considered:  $a_c = 0.15$  and  $0.20g$  that are close to the values of  $a_c$  obtained from the pseudo-static analyses [14]. The obtained permanent displacements are plotted in Fig. 3 against the ratio  $a_c/a_{max}$  together with the regression lines and the 90% non-exceedance confidence levels. The methods proposed by Whitman and Liao [11] and Ambraseys and Menu [12] provide similar results with maximum displacements less than about 10 cm. Larger displacements were obtained using the relationship proposed by Jibson [13]. In this method displacements are related to both Arias intensity and critical acceleration. Since artificial accelerograms are characterised by similar values of  $I_A = 3.52\text{--}4.67\text{ m/s}$  the results are mainly affected by changes in the ratio  $a_c/a_{max}$ . For

$a_c = 0.15g$  the displacement is about 25 cm, for  $a_c = 0.2g$  it is reduced to about 12 cm.

In addition to the simplified methods, the sliding block analysis was carried out considering rotational collapse mechanisms and assuming the potential sliding mass to behave as a rigid plastic body. The crest settlement  $S$ , computed for the four values of  $k_c = a_c/g$  labelled in Fig. 4, is similar, in both trend and magnitude, to that evaluated using the Whitman and Liao [11] and Ambraseys and Menu [12] relationships. In the figure the regression line and the 90% non-exceedance confidence levels are also shown.

### 3.2. Decoupled approach

Evaluation of earthquake-induced displacements can be also carried out following the decoupled approach, based on the assumption that the sliding block analysis can be decoupled from the ground response analysis of the earth structure. This approach represents a useful approximation for most earth structures and generally provides a conservative estimate of the seismic-induced permanent displacements [19,20].

Cascone and Rampello [10] carried out 1D and 2D ground response analyses of the dam assuming four values for the bedrock depth ( $z_B = 12, 25, 50$  and  $100\text{ m}$ ). Ten artificial accelerograms were used for the 1D response analysis, and five artificial accelerograms were used for the 2D response analysis. At the dam centre line, results from 1D and 2D analyses were in a fair agreement, with the exception of the top third of the dam where the 2D analyses predicted higher values of  $a_{max}$ . This was ascribed to both the 2D geometry of the problem and the wave focusing effects that increase as the top of the dam is approached. Fig. 5a–b shows the displacements computed using the sliding block method for two values of the critical seismic coefficient,  $k_c = 0.153$  and  $0.158$  [14], using the accelerograms provided by 1D and 2D ground response analyses at the centre of the sliding mass. The displacements obtained after 2D response analysis are greater than those evaluated after 1D analysis, attaining maximum values of about 40 cm. This is consistent with the larger amplification associated to the 2D geometry of the problem. The larger scatter observed after the 1D response analysis can be attributed to the larger set of input motions used in computations.

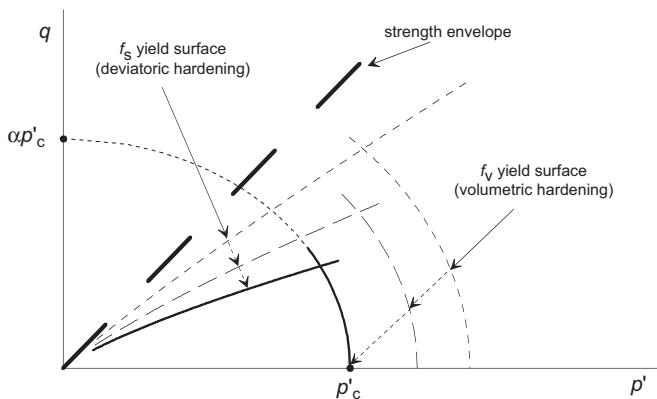


Fig. 6. Yield surfaces of the hardening soil model and their evolution.

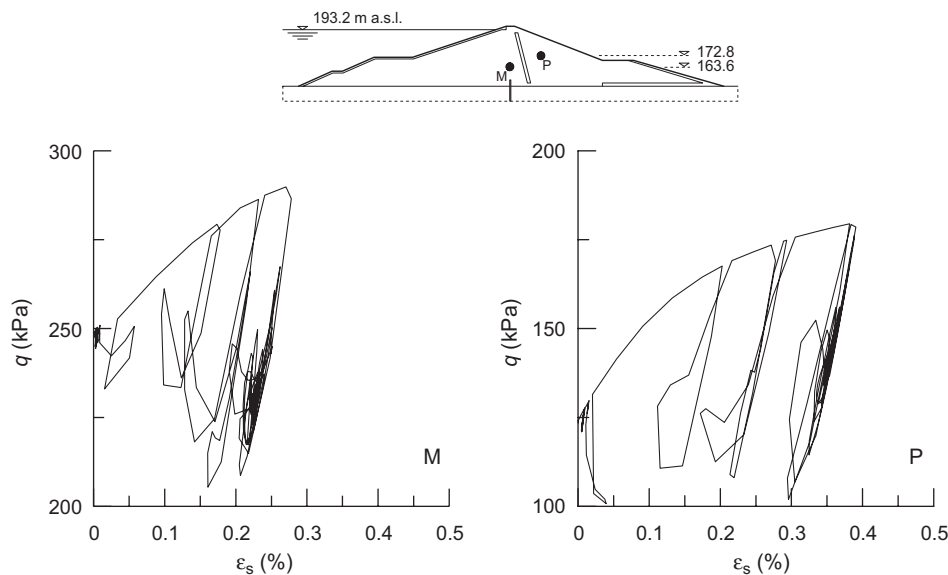


Fig. 7. Stress–strain response of selected soil elements of the dam during earthquake—real input accelerogram.

Among the simplified approaches, the method proposed by Jibson [13] was in a fair agreement with the decoupled approach in which the seismic ground response analyses were carried out under 2D conditions. Both methods yield permanent displacements similar to those computed with effective stress FE analyses, described in the next sections, which are shown for comparison in Figs. 3–5.

#### 4. Coupled analysis of the earth dam

##### 4.1. Soil model

An additional analysis of the seismic behaviour of the earth dam was performed using the finite element code *Plaxis* [21]. The

**Table 3**  
Stiffness coefficients

	OCR	R	m	n	S
Earth dam	1.0	1.0	–	0.75	1573
Alluvial silt	1.0	1.0	–	0.73	2155
Silty clay	1.5	1.3	0.19	0.73	2000

**Table 4**  
Mechanical properties for HS model

	c' (kPa)	φ' (deg)	E <sup>ref</sup> (kPa)	E <sup>ref</sup> /E <sub>50</sub> <sup>ref</sup>	TX-CIU tests E <sub>50</sub> <sup>ref</sup> /E <sub>oed</sub> <sup>ref</sup>	RC tests E <sub>50</sub> <sup>ref</sup> /E <sub>oed</sub> <sup>ref</sup>
Earth dam	30	30	119,400	10.9	1.25	2.43
Alluvial silt	7	33	149,200	18.3	1.16	2.49
Silty clay	60	25	145,500	10.4	0.78	2.24

mechanical behaviour of the soil was described using the constitutive model *Hardening Soil* (HS) [22,23]. This is an elastic–plastic rate independent model with isotropic hardening in which the elastic behaviour is defined by isotropic elasticity through a stress-dependent Young’s modulus:

$$E' = E'^{ref} \left( \frac{c' \cot \varphi' + \sigma'_3}{c' \cot \varphi' + p^{ref}} \right)^n \tag{1}$$

where  $\sigma'_3$  is the minimum principal effective stress,  $c'$  is the cohesion,  $\varphi'$  is the angle of shearing resistance,  $p^{ref} = 100$  kPa is a reference pressure, and  $E'^{ref}$  and  $n$  are model parameters.

The model has two yield surfaces  $f_s$  and  $f_v$  with independent isotropic hardening depending on deviatoric plastic strains  $\gamma^p$  and on volumetric plastic strains  $\epsilon_v^p$ , respectively (Fig. 6). The deviatoric hardening rule is related to parameter  $E'_{50}$ , while the volumetric one is controlled by parameter  $E'_{oed}$ . Both of them are given by expressions similar to Eq. (1) but, in contrast to  $E'$ , they are not used within a concept of elasticity.

The flow rule is associated for states lying on the surface  $f_v$ , while a non-associated flow rule is used for states on the surface  $f_s$ .

A feature of HS model is that under monotonic loading it can account for non-linear stress–strain behaviour, and for the occurrence of irreversible strains from the beginning of the loading process; this implies that for undrained conditions an increase of deviatoric stress  $q$  produces excess pore water pressure. Under cyclic loading conditions the model predicts plastic strains and excess pore water pressures only for cycles with increasing strain amplitude, that produce a progressive isotropic enlargement of the yield surfaces  $f_s$  or  $f_v$ . Conversely, for cycles of constant or decreasing amplitude, the model response becomes mainly linearly elastic with negligible hysteretic damping.

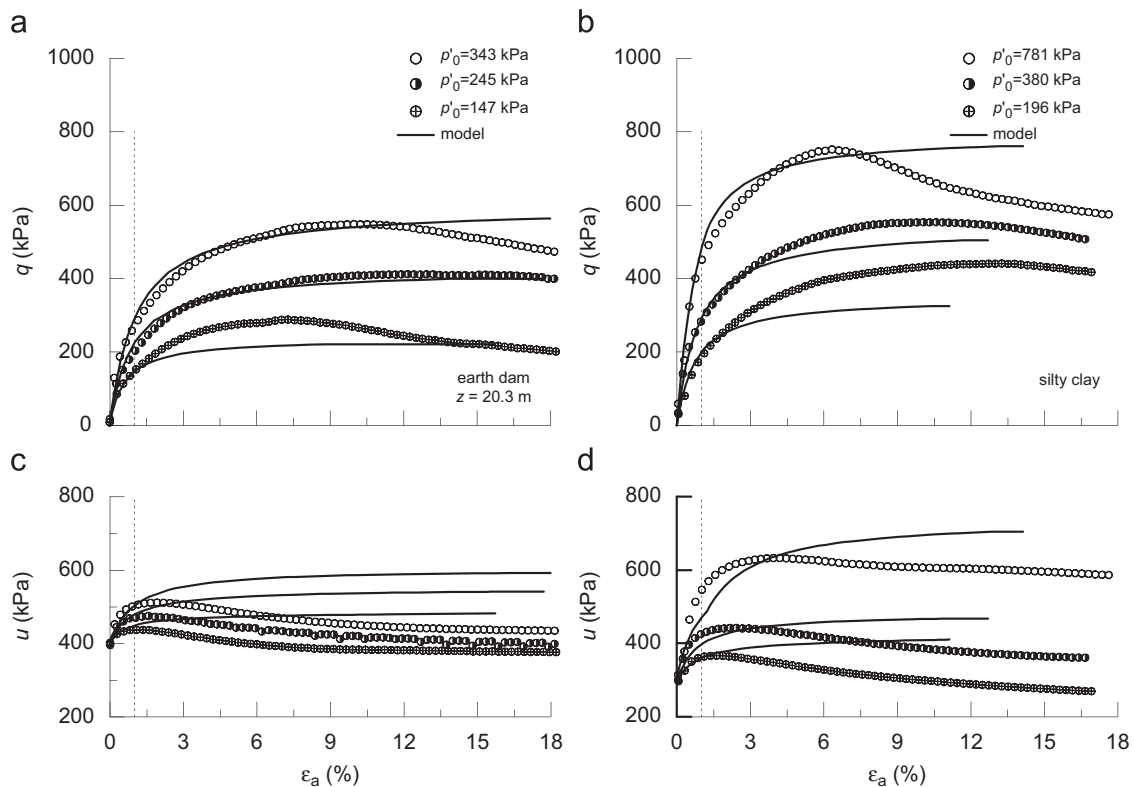


**Fig. 8.** Comparison between stress–strain response from TX-CIU tests and model simulations.

These features are shown in Fig. 7, in which the stress–strain response to earthquake loading is plotted for two soil elements of the earth dam. The curves show non-linear soil behaviour for increasing values of the deviator stress  $q$ , starting from small deviatoric strains  $\varepsilon_s$ , while the response is stiffer and nearly linear during the unloading–reloading cycles. The maximum value of  $q$  is attained at 6.5 and 7.1 s for soil elements  $M$  and  $P$ , respectively, that is towards the end of the strong motion phase of the input accelerogram.

#### 4.2. Parameter calibration

Since  $E'$  represents the tangent initial Young's modulus of the stress–strain curve, it has been related to the shear modulus at small strains  $G_0$ , as obtained from RC tests carried out on undisturbed samples retrieved at the site. Specifically, to evaluate the Young's modulus  $E'^{\text{ref}}$  at the reference pressure  $p_{\text{ref}} = 100$  kPa the relationship proposed by Viggiani [24] was used:

$$\frac{G_0}{p_r} = S \left( \frac{p'}{p_r} \right)^n R^m \quad (2)$$

where  $p'$  is the mean effective stress,  $p_r = 1$  kPa is a reference stress,  $R$  is the overconsolidation ratio defined as the ratio between the yield and the current mean effective stresses  $p'_y/p'$ , and  $S$ ,  $n$  and  $m$  are non-dimensional material constants. The stiffness exponents were estimated using the empirical relationships relating  $n$  and  $m$  to the plasticity index  $I_p$  [25], while the stiffness multiplier  $S$  was computed by introducing in Eq. (2) the experimental values of  $p'$ , applied in the RC tests, and the corresponding measured values of  $G_0$ . Once the stiffness coefficients were known (Table 3),  $E'^{\text{ref}}$  was determined assuming  $\nu' = 0.2$  (Table 4).

The remaining model parameters  $E'_{50}{}^{\text{ref}}$  and  $E'_{\text{oad}}{}^{\text{ref}}$  were calibrated according to the results of both consolidated undrained triaxial compression tests (TX-CIU) and consolidated undrained RC tests carried out on undisturbed samples retrieved with standard thin-walled open tube samplers.

Fig. 8 shows the comparison between model simulations and test results for triaxial tests carried out on samples retrieved from the earth dam and the foundation soils. It was found that a good agreement for the stress–strain curves and the generated excess pore water pressures can be obtained using the ratios of  $E'^{\text{ref}}/E'_{50}{}^{\text{ref}}$  and  $E'_{50}{}^{\text{ref}}/E'_{\text{oad}}{}^{\text{ref}}$  listed in Table 4 and a value for the angle of dilatancy at failure  $\psi = 0$ . Table 4 also lists the values of effective cohesion  $c'$  and angle of shearing resistance  $\varphi'$  adopted for calibrating the test results; these are the same values used in the displacement-based approach. A fair agreement is obtained for the pre-failure stress–strain and excess pore water pressure curves for the range of deviatoric strain involved during the earthquake loading ( $\leq 1\%$ ).

In Fig. 9 the experimental values of non-dimensional shear modulus  $G/G_0$  and excess pore water pressure ratio  $\Delta u/p'_0$  obtained from RC tests are compared with the corresponding values computed using the HS model and simulating a simple shear test with increasing strain amplitude. Higher values of the ratio  $E'_{50}{}^{\text{ref}}/E'_{\text{oad}}{}^{\text{ref}}$  were needed for best fitting the experimental results with respect to those required for calibration of monotonic TX-CIU tests. The secant stiffness predicted by the model, shown with a solid line in the figure, decreases progressively as strains increase for values of  $\varepsilon_s > 0.002\%$ , plotting slightly above the experimental data. The computed values of excess pore water pressure are in a fair agreement with the experimental values for the alluvial silt and the silty clay, while some overestimate of  $\Delta u$  is obtained for the earth dam for  $\gamma > 0.06\%$ . Assuming the volumetric threshold  $\gamma_v$  to correspond to a ratio  $\Delta u/p'_0 = 0.05$ , significant pore water pressure build-up can be anticipated to occur for

values of  $\gamma$  larger than about 0.2% in the earth dam and about 0.1% in the foundation soil.

It is worth mentioning that the triaxial-based soil parameters provide a steeper decay of soil stiffness with shear strain than that obtained from RC tests. This may result from having calibrated the model parameters  $E'_{\text{oad}}{}^{\text{ref}}$  and  $E'_{50}{}^{\text{ref}}$  on triaxial test results based on external measurements of axial strain that are known to underestimate the shear stiffness at small strains; as a consequence a steep decrease is obtained when relating the small-strain shear modulus  $G_0$  to values of  $G$  derived from TX-CIU tests. FE analyses were carried out using the TX-based parameter calibration that should yield larger dam displacements. As discussed in the following sections a few analyses were repeated using RC-based model parameters to evaluate the influence of different model

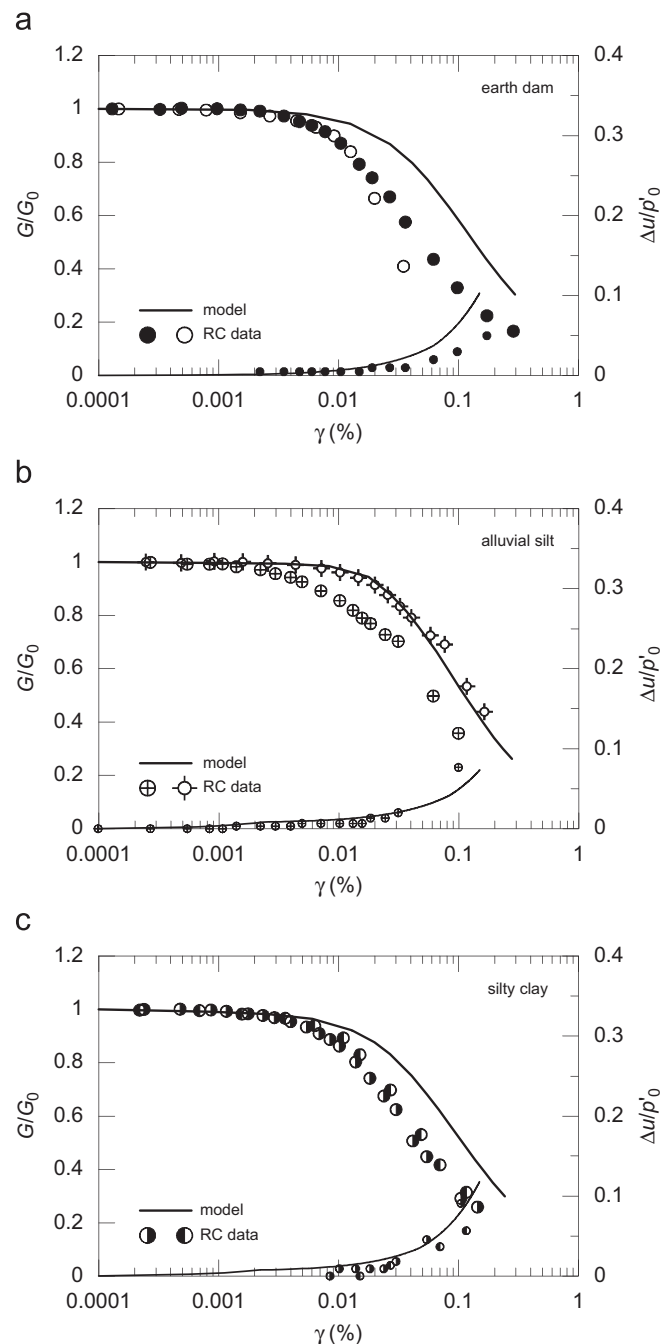


Fig. 9. Comparison between stiffness decay observed in RC tests and model simulations.

calibration on the overall response of the earth dam to earthquake loading.

4.3. FE model

The FE analyses were carried out under plane strain conditions using triangular six-noded elements with three-point Gaussian integration, a second-order polynomial interpolation for the displacements and a first-order interpolation for the pore water pressure, for a total of 3811 elements (Fig. 10). The FE mesh extended horizontally to about 400 m from the axis of the earth dam and vertically down to a depth of 300 m, where the influence of the earth dam is negligible.

In static analyses vertical boundaries were restrained in the horizontal direction, while displacements of the bottom of the mesh were restrained both horizontally and vertically. In seismic analyses absorbent boundaries were adopted along the vertical and horizontal edges of the FE mesh and seismic loading was applied imposing the selected input accelerograms at the considered bedrock depth. The absorbent boundaries are based on the scheme described by Lysmer and Kuhlemeyer [26] in which an increase in stress on the boundary is absorbed independently of the frequency of the incident waves.

To avoid numerical distortion of the propagating wave during the dynamic analysis, the maximum height of elements of the dam ( $\Delta l_{max} = 3$  m) and of the alluvial silt layer ( $\Delta l_{max} = 6$  m) was smaller than  $\frac{1}{6}$  of the wavelength  $\lambda_{min}$  associated with the highest frequency component of the input wave  $f_{max}$  [27]. A value of  $f_{max} = 10$  Hz was fixed since negligible energy content is associated to higher frequencies (Fig. 2); the input accelerograms were then low-pass filtered removing frequency components higher than 10 Hz.

It was pointed out that, for strain cycles of constant or decreasing amplitude, the soil model predicts negligible hysteretic damping. Therefore, the overall capability of the model to dissipate energy was deemed insufficient and additional viscous damping had to be introduced in the analysis using the Rayleigh formulation.

A viscous damping ratio  $\xi = 10\%$  was selected as an average lower bound of the equivalent damping obtained by Cascone and Rampello [10] from 1D and 2D equivalent linear analyses of the earth dam. Values of Rayleigh coefficients  $\alpha_R = 1$  and  $\beta_R = 0.01$  were obtained to ensure a nearly constant damping in the range of predominant frequencies for the problem at hand,  $f = 0.8\text{--}2.4$  Hz.

The time integration in *Plaxis* is carried out using the Newmark scheme: standard values of constants  $\alpha = 0.25$  and  $\beta = 0.50$  were adopted to obtain an unconditionally stable solution. Time integration was carried out using the same time step  $\Delta t = 0.01$  s adopted for the input accelerograms.

4.4. Back analysis of earth dam construction

Prior to studying the dam response to earthquake loading, the construction of the earth dam was simulated to reproduce the initial state of effective stress. Comparison of dam settlements observed during and after construction with the computed ones permitted to check the constitutive model calibration.

The pore water pressure before dam construction was assumed hydrostatic with the water table at the ground surface and the initial state of effective stress was computed using values of the coefficient of earth pressure at rest  $K_0$  written in the form

$$K_0 = (1 - \sin \varphi') \text{OCR}^{\sin \varphi'} \tag{3}$$

where OCR is the overconsolidation ratio before the earth dam construction. This was estimated using the OCR profile obtained from the oedometer tests performed in the supplementary geotechnical investigation, carried out about 25 years after the end of the dam construction; values of  $K_0$  and OCR used in the analyses are listed in Table 5.

Modelling the earth dam history included the staged construction of the dam, considered as a drained process, via the progressive activation of 19 rows of elements about 2.5 m thick, the impoundment of the reservoir and the associated steady state seepage flow through the dam.

Model calibration was checked against the settlements measured during the dam construction via four extensometers

Table 5  
OCR and  $K_0$  values

Soil	$z$ (m)	Current		Before dam construction		
		$\sigma'_{v0}$	OCR	$\sigma'_{v0}$	OCR	$K_0$
Alluvial silt	6.0	752.3	1.5	60.0	18.8	2.31
Silty clay	18.5	847.3	2.0	185.0	9.2	1.49
Silty clay	37.5	1010.0	1.5	375.0	4.0	1.03
Silty clay	74.6	1300.0	1.3	746.0	2.3	0.61
Silty clay	199.6	2400.0	1.3	1996.0	1.6	0.59

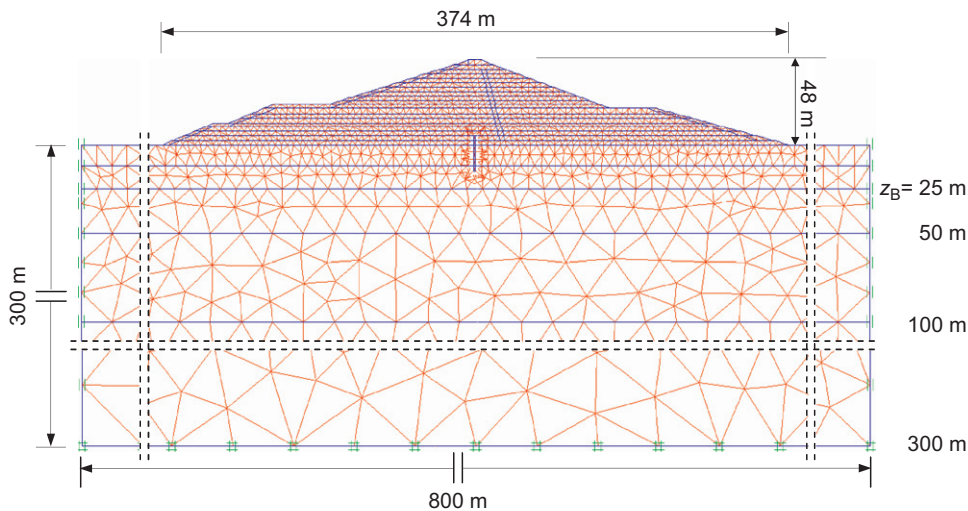


Fig. 10. Mesh used in the numerical analyses.

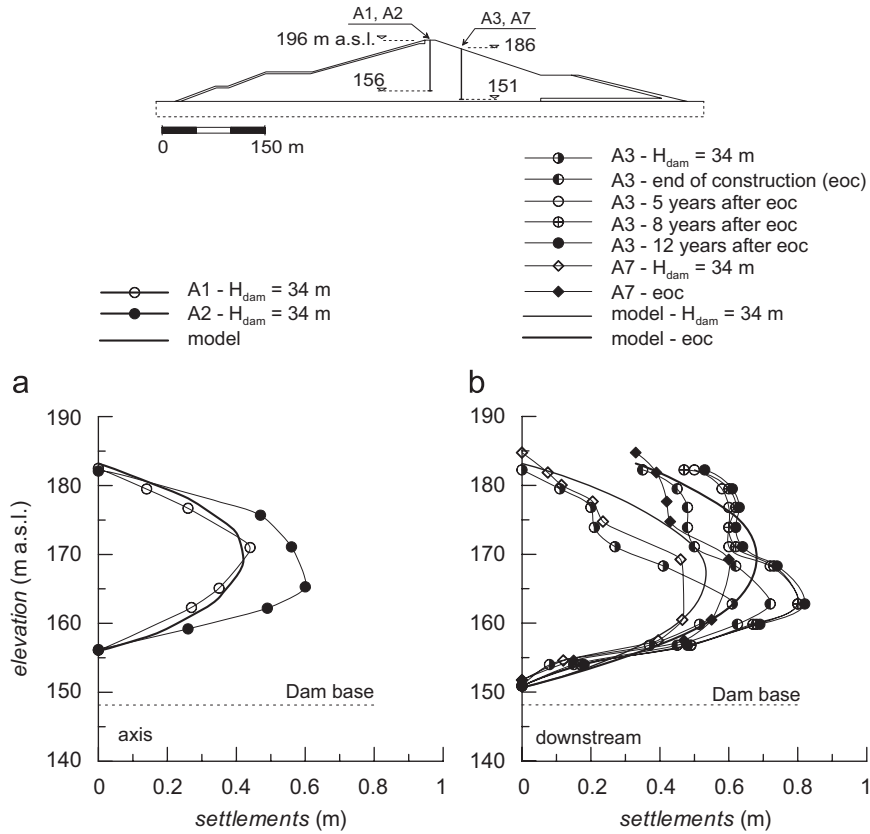


Fig. 11. Observed and computed settlement profiles: (a) extensometers A1 and A2 and (b) extensometers A3 and A7.

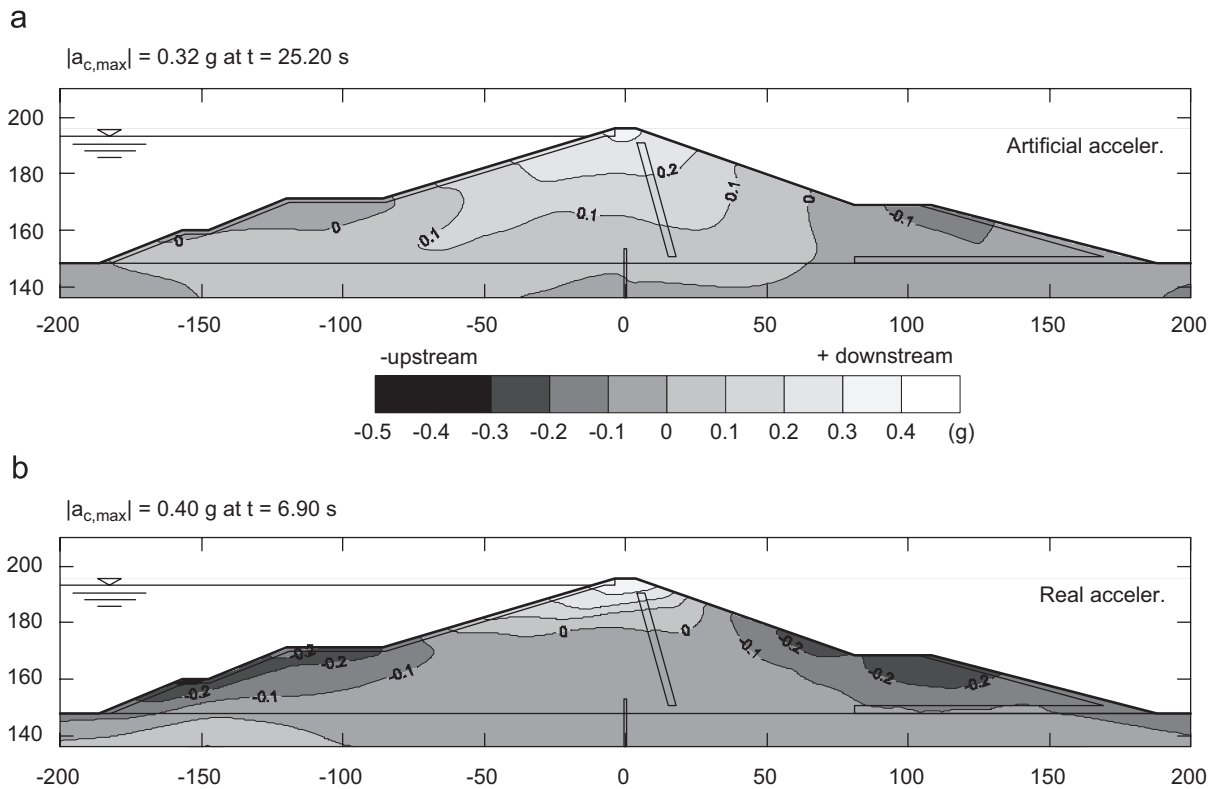


Fig. 12. Contour lines of horizontal acceleration at the time when maximum acceleration is reached at the crest of the dam for artificial (a) and real (b) accelerograms ( $z_B = 50$  m).

installed at the centre line and in the downstream slope of the dam (see Fig. 1). The observed settlement profiles are shown in Fig. 11; they were obtained following the procedure by

Poulos et al. [28] in which it is assumed that the foundation soil is incompressible. Fig. 11a shows the settlement profiles along two vertical axes (A1 and A2) through the crest of the dam at a stage when the dam was not yet completed ( $H = 34$  m), while Fig. 11b shows profiles along two vertical axes located on the downstream slope of the dam (A3 and A7). Measurements from extensometer A3 span over a long period of time during the dam construction and after the dam was completed in 1975. The measured settlement profiles attain the maximum value at approximately mid-height, consistently with 1D analytical and 2D numerical results of homogeneous earth dams (e.g. [29]). The observed slight deviation from the theoretical parabolic pattern might be attributed to the presence of large banks on both sides of the embankment. In addition, the observed increase in settlements at the top of extensometers can be attributed to the construction of the overlying portion of the dam and to the consolidation process of the dam after the end of construction.

**Table 6**  
Maximum acceleration and amplification ratios at the dam crest

Input	$z_B$	$a_{br}$ (g)	$a_{base}$ (g)	$a_{c,max}$ (g)	$a_{c,max}/a_{base}$	$a_{c,max}/a_{br}$
Artificial	25	0.32	0.29	0.40	1.36	1.27
	50	0.30	0.28	0.32	1.14	1.08
	100	0.29	0.19	0.24	1.25	0.83
	300	0.27	0.10	0.17	1.63	0.62
Real	25	0.28	0.23	0.42	1.83	1.51
	50	0.29	0.18	0.40	2.22	1.37
	100	0.27	0.14	0.27	1.87	0.99
	300	0.27	0.08	0.21	2.67	0.77

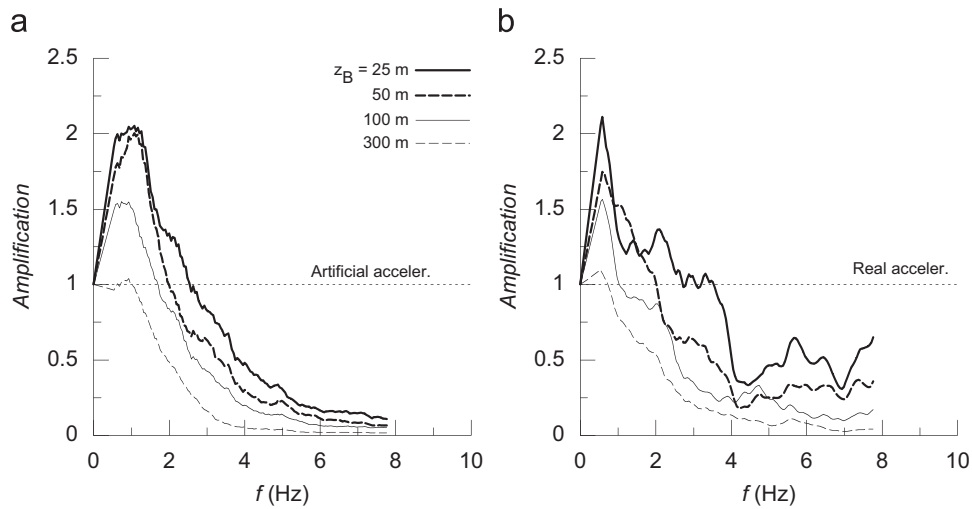


**Fig. 13.** Amplification functions for artificial and real accelerograms.

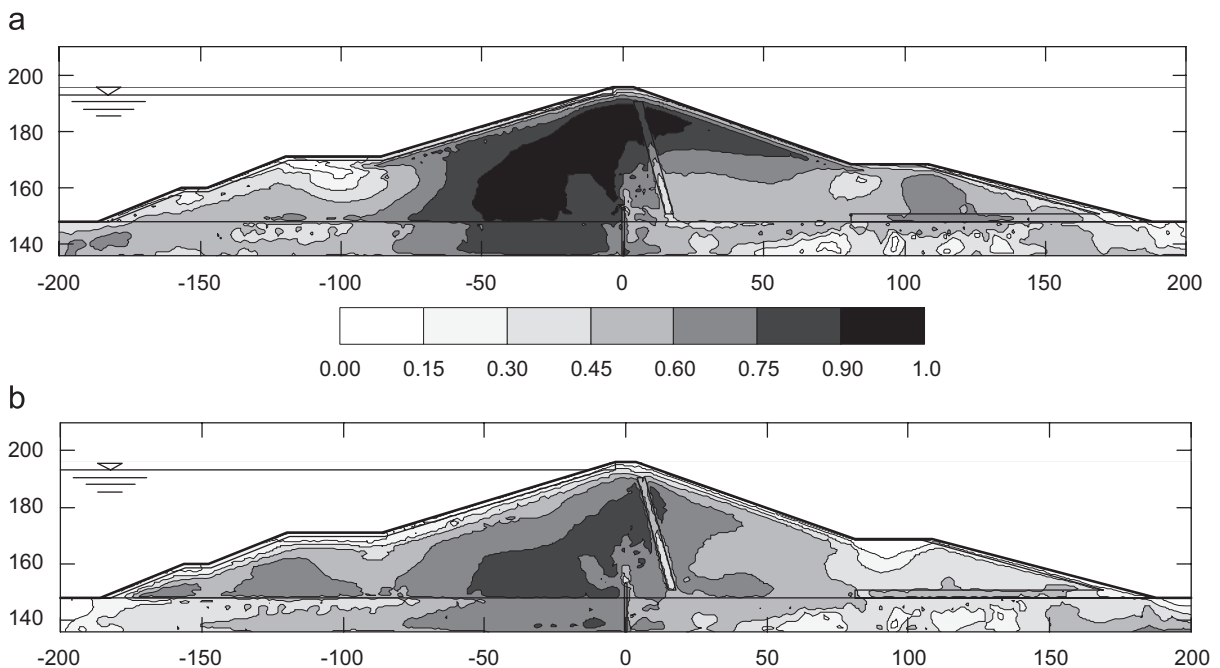


**Fig. 14.** Contour lines of mobilised shear strength  $t/t_{max}$  for the artificial accelerogram ( $z_B = 50$  m): (a) at the time when  $a_{max}$  is reached at the crest and (b) at the end of earthquake.

The computed settlement profiles shown with solid lines in Fig. 11, embody the observed behaviour, capturing with a fair agreement the overall deformation pattern of the dam during and after construction. In addition to a fair estimate of the deformation of the dam body, the settlement computed at the base of the dam centre line  $w_{comp} = 1.5$  m is in good agreement with the settlement  $w_{meas} \approx 1.6$  m measured 11 years after the end of construction, indicating a satisfactory choice of the input stiffness parameters for both the dam and the foundation soils.

5. Dynamic analysis

Coupled effective stress dynamic analyses were carried out for both the artificial and the real accelerograms. The analyses were prolonged till 60 s, in order to allow the velocity field to vanish, regardless the actual duration of the accelerograms. Analysis results are presented in the following sections in terms of acceleration field and of stress, strain and displacement fields.

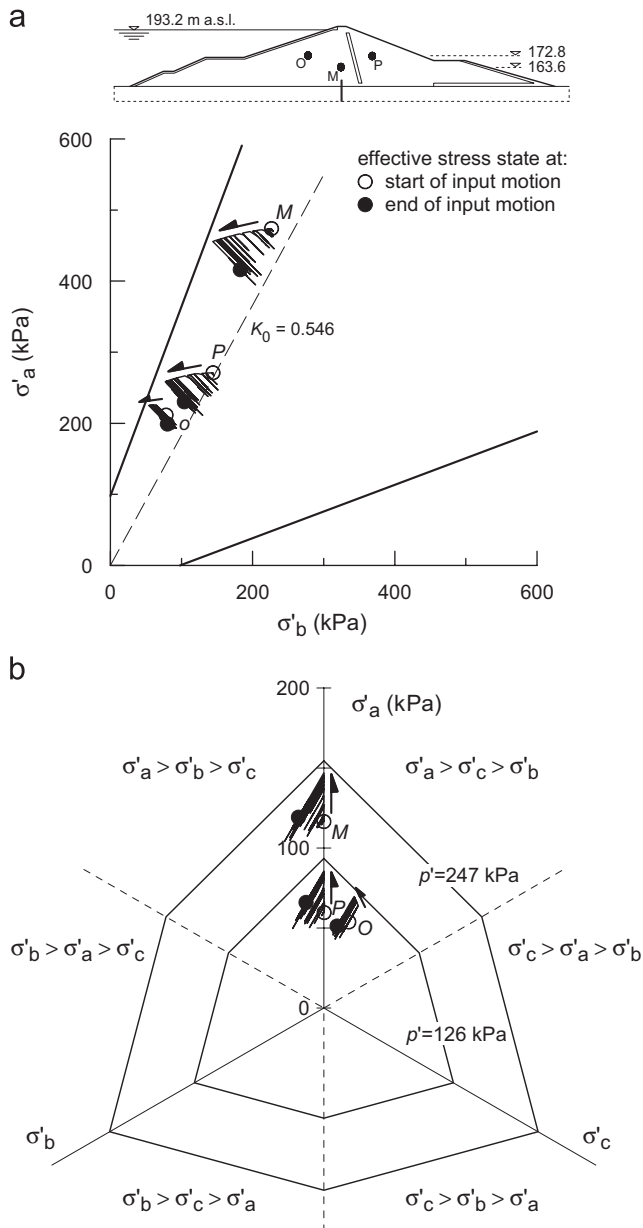


Fig. 15. Undrained stress paths for selected soil elements in the dam.

5.1. Acceleration field

Fig. 12 shows the acceleration contours obtained, for  $z_B = 50$  m, at the time when maximum acceleration is reached at the crest of the dam. For the artificial accelerogram, the acceleration field is gradually increasing with elevation from about 0.1 to 0.32g, with zones of higher acceleration extending towards the upstream slope (Fig. 12a); the direction of shaking is about uniform throughout the dam. Conversely, for the real accelerogram, the acceleration field is not in phase, acceleration being directed downstream at the crest and upstream at the banks. Along the centre line the acceleration attains low values from the base to the upper third of the dam and increases abruptly thereafter (Fig. 12b).

Table 6 lists the values of the peak acceleration of the input motion at the bedrock,  $a_{br}$ , the maximum acceleration at the base and at the crest of the dam,  $a_{base}$  and  $a_{c,max}$ , as obtained from the numerical analyses, and the ratios of crest to base ( $a_{c,max}/a_{base}$ ) and crest to bedrock ( $a_{c,max}/a_{br}$ ) maximum accelerations. The maximum accelerations at the base and at the crest of the dam decreases for increasing depth of the bedrock, and the values of  $a_{c,max}$  obtained using the real motion are slightly larger than those obtained using the artificial accelerogram. The ratio  $a_{c,max}/a_{base}$  is in the range of 1.8–2.7 and 1.1–1.6 for the real and artificial motion, respectively. Maximum values of the amplification ratio ( $a_{c,max}/a_{base}$ ) refer to weak motions ( $a_{base} < 0.15g$ ), propagating from deep bedrock ( $z_B = 100$ – $300$  m), that mostly deform the dam

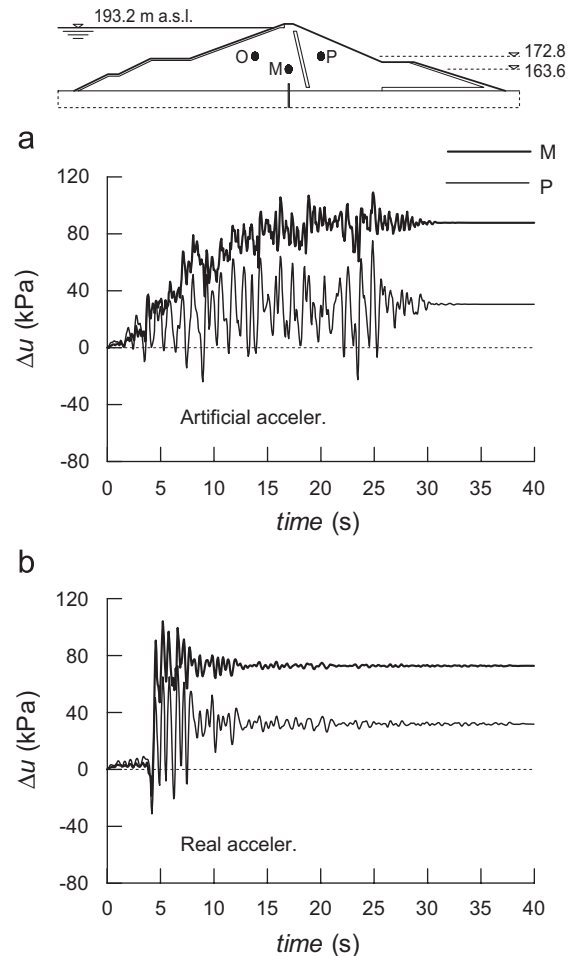


Fig. 16. Pore water pressure build-up computed for artificial (a) and real (b) accelerograms in selected soil elements of the dam ( $z_B = 50$  m).

in the range of small shear strains. Values of amplification ratio as large as 1.8 and 2.2 were obtained using the real accelerogram for  $z_B = 25$  and 50 m; smaller values of the ratio were obtained using the artificial accelerogram due to the significantly higher accelerations at the base of the dam. For a deep bedrock the ratio  $a_{c,max}/a_{br}$  is minimum and smaller than unity, denoting a global de-amplification of the original input motion; conversely, for shallower depths of the bedrock ( $z_B = 25$ –50 m) the ratio  $a_{c,max}/a_{br}$  is greater than unity showing a net amplification of the original input motion.

Fig. 13 shows the amplification functions obtained as the ratio between the Fourier spectra of the crest and the outcropping motions. Amplification functions relative to the artificial motion exhibit a plateau in the range of frequencies of 0.5–1.4 Hz for all the considered bedrock depths (Fig. 13a). Maximum amplification is about 2 for  $z_B = 25$  and 50 m and 1.5 for  $z = 100$  m occurring for a frequency of about 1 Hz; for  $z_B = 300$  m no amplification is observed. Amplification functions relative to the real motion exhibit a sharp spike, maximum amplification of 1.1–2.1 being attained for a frequency of about 0.6 Hz (Fig. 13b). Comparing the amplification functions with the Fourier amplitude spectra shown in Fig. 2c it is apparent that in the range of frequencies of maximum amplification the artificial accelerogram is characterised by large amplitudes, while the real accelerogram is characterised by low amplitudes.

5.2. Stress and strain fields

The stress state within the dam embankment was evaluated using the mobilised shear strength  $t/t_{max}$  where  $t = (\sigma'_1 - \sigma'_3)/2$  and  $\sigma'_1$  and  $\sigma'_3$  are the maximum and minimum principal effective stresses; as values of  $t/t_{max}$  approach unity, the full shear strength of the soil is attained.

Fig. 14 shows the contour lines of mobilised shear strength obtained using the artificial accelerogram at  $z_B = 50$  m as input motion. At the time when the maximum acceleration is reached at the crest, values of  $t/t_{max}$  in the range of 0.9–1.0 are obtained in

the central portion of the embankment, to the left of the central drain, while most of the earth body experiences values of  $t/t_{max}$  smaller than 0.6 (Fig. 14a). At the end of the seismic shaking the mobilised shear strength reduces to 0.6–0.75 in the central portion of the dam while it is  $t/t_{max} < 0.45$  throughout the rest of the embankment (Fig. 14b).

For the same bedrock depth, Fig. 15 shows the stress paths of soil elements *O* and *P*, located at the elevation of the banks (172.8 m a.s.l.) at about 29 m from the dam centre line, and element *M*, located along the centre line, about 10 m below (163.8 m a.s.l.).

Subfixes *a*, *b* and *c* in the figure denote principal directions of stress. Direction *c* is normal to the plane of deformation; directions *a* and *b*, contained in the plane of deformation, are about the vertical and the horizontal directions at the beginning of earthquake loading, but can rotate during the seismic event. Then, principal stresses  $\sigma'_a$ ,  $\sigma'_b$  and  $\sigma'_c$  are not ordered according to their value.

During earthquake loading the soil elements experience a progressive decrease of horizontal effective stress with only minor reduction of vertical stress, approaching the condition of active limit equilibrium (Fig. 15a). At the end of the seismic shaking, the stress state of the soil elements is characterised by lower effective stresses due to the excess pore water pressure developed during the earthquake loading. The same stress paths are also represented on the deviatoric stress plane (Fig. 15b) in which distances from the origin are equal to the octahedral shear stress

$$\tau_{oct} = \frac{1}{3}[(\sigma'_a - \sigma'_b)^2 + (\sigma'_b - \sigma'_c)^2 + (\sigma'_c - \sigma'_a)^2]^{1/2} \quad (4)$$

In this plane, the initial stress state of elements *M* and *P* are close to axisymmetric conditions; during shaking the stress states of the soil elements undergo a progressive increase in the octahedral shear stress remaining in the sector  $\sigma'_a > \sigma'_b > \sigma'_c$  in which  $\sigma'_a$  and  $\sigma'_c$  are the maximum and the minimum principal effective stresses. Stress path of soil element *O* plots within the sector  $\sigma'_a > \sigma'_c > \sigma'_b$  in which  $\sigma'_a$  and  $\sigma'_b$  are the maximum and minimum principal effective stresses. During the earthquake loading, the stress paths approach the Mohr–Coulomb strength envelopes

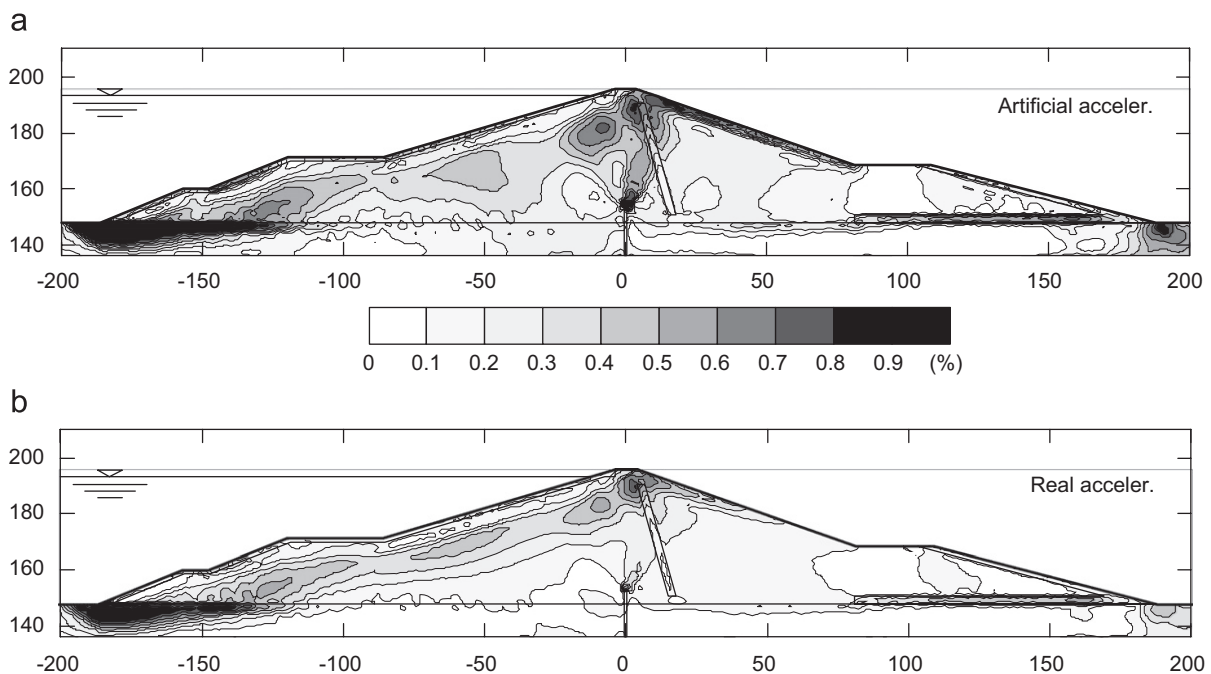


Fig. 17. Contour lines of deviatoric strain  $\epsilon_s$  at the end of earthquake motion for artificial (a) and real (b) accelerograms ( $z_B = 50$  m).

relevant to elements *O* and *P* ( $p'_{\min} = 126$  and  $137$  kPa) and to element *M* ( $p'_{\min} = 247$  kPa) without reaching failure conditions.

Fig. 16 shows typical trends of pore water pressure build-up computed in soil elements *M* and *P* during seismic shaking using both the artificial and the real accelerograms. Values of excess pore water pressure obtained in the soil element *M* located in the lower portion of the dam are higher than those computed downstream, in point *P*. For any of the bedrock depths considered in the analyses, a larger rate of pore water pressure build-up was obtained using the real accelerogram, consistently with the shapes of the applied acceleration time histories.

Fig. 17 shows the contours of the deviatoric strain

$$\epsilon_s = \frac{\sqrt{2}}{3} \left[ (\epsilon_x - \epsilon_y)^2 + \epsilon_x^2 + \epsilon_y^2 + \frac{3}{2} \gamma_{xy}^2 \right]^{1/2} \quad (5)$$

obtained applying the input motions at a bedrock depth  $z_B = 50$  m.

Both artificial and real accelerograms yield values of shear strain  $\epsilon_s \geq 0.8\%$  in zones of limited extension located at the upstream toe and at the crest of the dam. In most of the embankment the shear strain is in the range of 0.1–0.3%, resulting greater than the volumetric threshold observed in the RC test results ( $\approx 0.2\%$ ) only locally.

### 5.3. Displacement field

Fig. 18 shows vertical and horizontal displacements at different elevations along the centre line of the dam cross section, as obtained by applying the input motion at the bedrock depth  $z_B = 50$  m. Vertical displacements decrease with elevation being maximum at the crest and minimum at the base of the dam: using the artificial accelerogram as input motion the crest and base displacements were 25 and 6.5 cm, respectively (Fig. 18a), while for the real accelerogram the corresponding values were 16 and 4 cm (Fig. 18b). Permanent displacement results from plastic strains that accumulate during the earthquake because of progressive plastic loading of the yield surfaces  $f_s$  and  $f_v$  and of the instantaneous mobilisation of the available shear strength. Therefore, the final permanent displacements are influenced by the duration of the strong motion phase of the accelerograms.

The same differences in the dam response can be observed in Fig. 18c–d showing the horizontal displacement time histories computed at the same four locations in the dam using both the artificial and the real accelerograms. The displacement response to the artificial motion does not exhibit significant variations within the dam body, horizontal displacement being directed towards upstream with a maximum displacement of about 22 cm

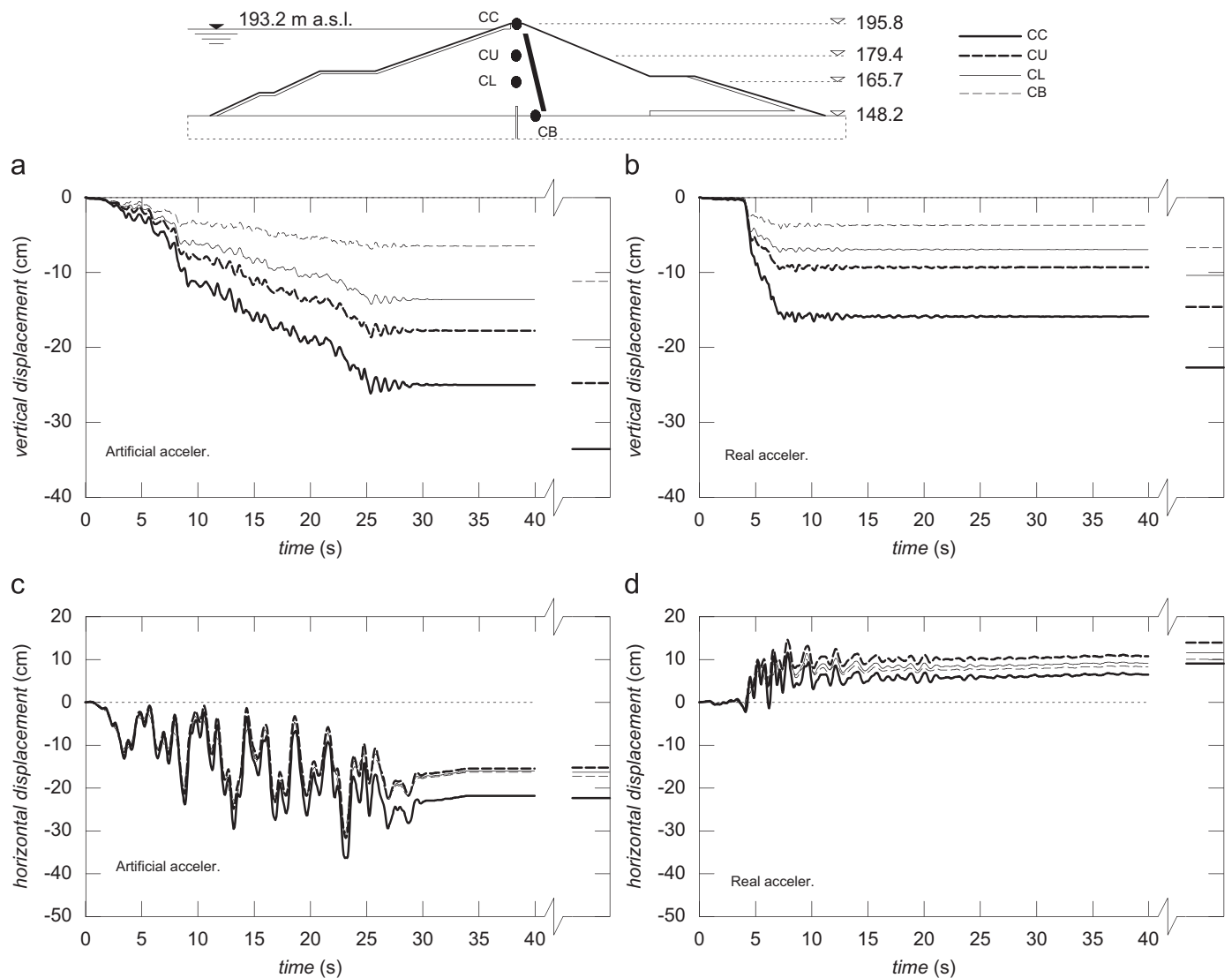


Fig. 18. Vertical and horizontal displacements computed for artificial (a–c) and real (b–d) accelerograms along the centre line of the dam cross section for  $z_B = 50$  m.

at the crest (Fig. 18c). The displacement time history is very irregular and is characterised by sharp alternate peaks, denoting a back and forth motion until the end of the external excitation. The displacement time histories obtained using the real accelerogram are more regular and all the selected points move in the downstream direction, with displacements in the range of 7–11 cm (Fig. 18d).

Fig. 19 shows the influence of the bedrock depth on the vertical displacements computed at the crest of the dam. In the case of the artificial motion (Fig. 19a) the maximum permanent displacement is in the range of 22–30 cm and decreases for increasing  $z_B$ . Displacements of 8–16 cm are obtained when applying the real motion (Fig. 19b), with the maximum value computed for a bedrock depth  $z_B = 50$  m. This may be ascribed to a close coupling occurring in this case among the predominant periods of the input motion ( $\approx 0.65$  s), the 50 m thick soil layer ( $\approx 0.74$  s) and the earth dam ( $\approx 0.57$  s).

Figs. 18 and 19 also show the long-term values of displacement computed at the end of the consolidation analyses. Increments of vertical displacement at the crest of the dam, due to pore water pressure dissipation, are of 22–40%, with the maximum value attained for the real motion (Fig. 19). The corresponding increments of horizontal displacement are nearly negligible for both the artificial and the real accelerograms.

Vertical and horizontal displacements relative to the base of the dam were computed to obtain the displacement profiles of the dam centre line (Fig. 20). Vertical displacement profiles evaluated using the artificial motion (Fig. 20a) are about two times larger than those obtained using the real accelerogram (Fig. 20b). The

horizontal displacement profiles for the two input motions are qualitatively similar with those typical of a second mode response of a linear elastic inhomogeneous shear beam [30]. Differences in the horizontal displacement profiles are noticeable in the upper third of the dam (Fig. 20c–d). As a general rule, horizontal and vertical displacements along the dam centre line are increasing with decreasing bedrock depth. However, it can be observed that for  $z_B = 25$  and 50 m, the displacement profiles obtained for the real motion are almost coincident, possibly due to the discussed coupling of predominant periods occurring for  $z_B = 50$  m. The overall deformation pattern of the earth dam mainly consists in dam compaction associated with lateral deformation.

## 6. Discussion and conclusions

In the different methods of analysis adopted to study the seismic performance of the Marana Capacciotti earth dam, the soil behaviour was described using different constitutive assumptions, from the simple rigid-perfectly plastic behaviour assumed in the sliding-block analyses, to the visco-elastic model adopted in the total stress ground response analyses, to the elastic-plastic model with isotropic hardening used in the effective stress FE dynamic analyses, this requiring an increasing number of input parameters.

The constitutive model used in the FE analyses is capable to reproduce to some extent non-linear soil behaviour with development of irreversible plastic strains from the early beginning of the loading path.

Parameter calibration for FE analyses was based on TX test results that yielded a steeper decrease of shear stiffness with shear strain than that obtained from RC tests. Fig. 21 shows a comparison between the earth dam displacements obtained using TX-based (thick lines) and RC-based (thin lines) calibrations of model parameters and using the real accelerogram applied at  $z_B = 50$  m. Fig. 21a shows the influence of calibration on vertical displacements of points located along the centre line of the dam. Using the results of RC tests to calibrate model parameters, vertical displacements are 29–98% of those computed after TX-based calibration; differences are larger for deeper points in the dam where the absolute values of displacement are smaller. Fig. 21b shows the influence of calibration on horizontal displacements of points located on the slopes of the dam: displacements are nearly coincident for points resting on the downstream slope, while for points located on the upstream slope the RC-based displacements are larger than those obtained after TX-based calibration, being however less than about 10 cm. As it could be anticipated, different results are obtained using different sets of experimental data to calibrate model parameters, though, for the case considered in this study, the overall pattern of behaviour of the dam was not altered substantially.

The maximum acceleration profiles obtained from the effective stress FE analyses are shown in Fig. 22 together with the range of results found in the literature [6–9,31–33], and with the results obtained from 2D equivalent linear analyses of the dam [10];  $a_{(z=12\text{ m})}$  in the figure is the maximum acceleration at the contact between the alluvial soil and the underlying deposit of stiff clay ( $z = 12$  m). A fair agreement among results is observed, though smaller amplification ratios are obtained for the coupled effective stress analyses carried out using the artificial accelerogram, possibly due to more significant non-linear effects than those reproduced in the equivalent linear method. For both real and artificial accelerograms, the acceleration profiles define a narrow band. For the two profiles obtained assuming  $z_B = 300$  m a slightly different trend is observed with larger amplification in

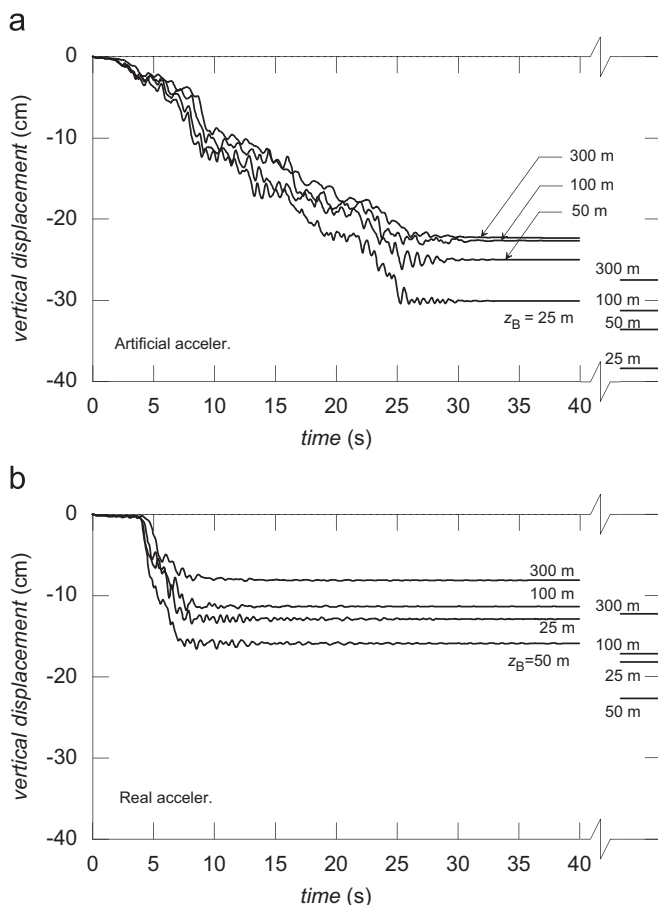


Fig. 19. Influence of bedrock depth  $z_B$  on vertical displacements computed at the crest of the dam for artificial (a) and real (b) accelerograms.

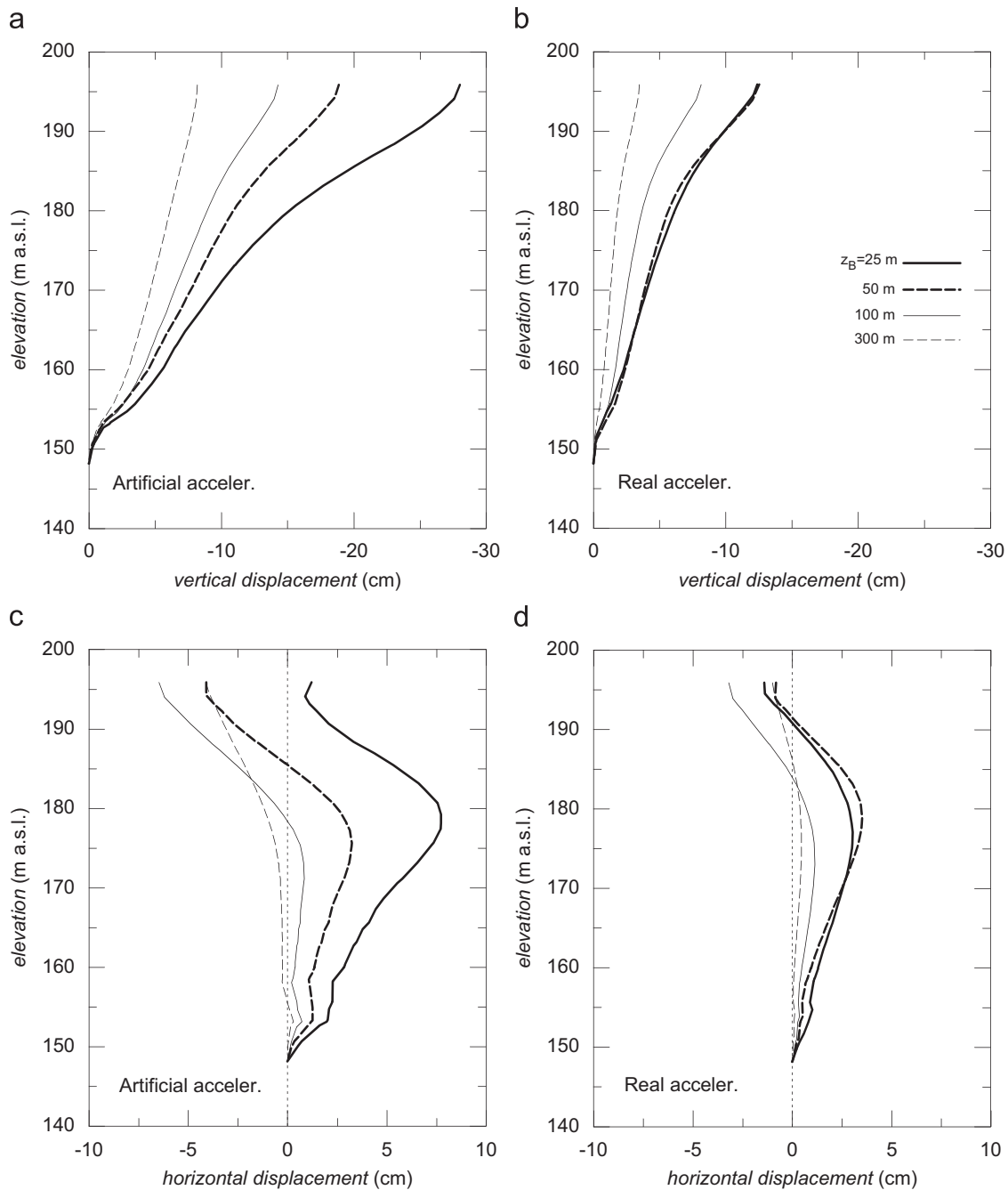


Fig. 20. Vertical and horizontal displacement profiles computed along the dam centre line for artificial (a–c) and real (b–d) accelerograms.

the dam. In these cases, large amplifications are attributable to a mainly elastic response of the dam to the weak motions resulting from propagation from a deep bedrock, the maximum acceleration at the crest being smaller than those obtained for the other bedrock depths (Table 6).

The acceleration field computed by the FE analyses (Fig. 12) is in a fair agreement with the contour lines of  $a_{\max}$  evaluated by the 2D total stress FE analyses carried out via the linear equivalent method [10]. Acceleration contours in Fig. 12 refer to the time instant when acceleration is maximum at the crest. Consistently with the acceleration fields predicted by equivalent linear analyses [6,10] and non-linear analyses [34], maximum accelerations, as large as 0.28 and 0.36g, occurred at the slopes and close to the banks; this result can be ascribed to lack of confinement and geometrical effects that amplify the dam

response because of the larger participation of high frequency motion components [34].

The artificial accelerograms used in the analyses were characterised by a long duration of the stationary strong motion phase and by a broadband frequency content, resulting in larger displacements of the earth dam compared with those induced by the real input motions. In fact, spectrum compatible time histories match the entire spectrum within a prescribed tolerance, so that all periods are subjected to the full design seismic action and displacement response may therefore be overestimated [2].

Displacements of the earth dam generally decreased as the bedrock depth increased, due to the filtering effects of the foundation soil, although some amplification was observed when using real accelerograms applied at shallow depths ( $z_B = 25\text{--}50\text{ m}$ ); for these cases some coupling among the fundamental

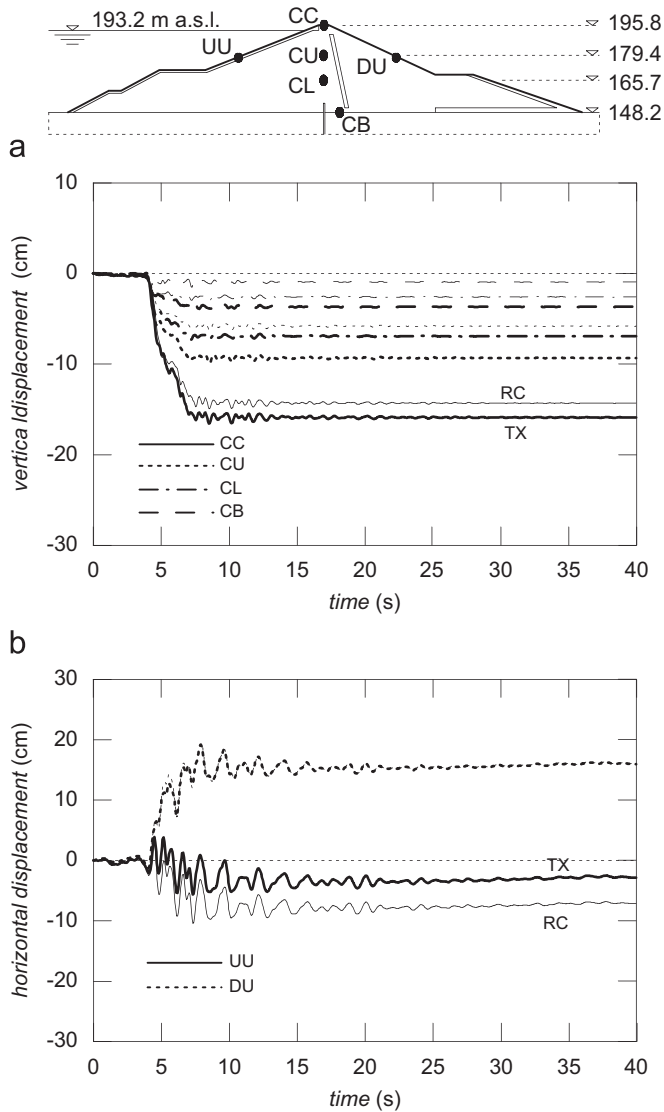


Fig. 21. Influence of parameter calibration on vertical (a) and horizontal (b) displacements computed using the real accelerogram at  $z_B = 50$  m.

frequencies of input motions, foundation soil and earth dam possibly occurred.

Effective stress FE analyses permitted to evaluate post-seismic stability of the earth dam. To this purpose, undrained analyses were carried out in terms of effective stresses, accounting for the pore pressure build-up induced by earthquake loading. Stability conditions were evaluated by progressively reducing the effective cohesion  $c'$  and the angle of shearing resistance  $\phi'$  by a factor  $F$  until large displacements of the dam were obtained. Using this procedure the factor of safety was estimated as the value corresponding to a change in the curvature of the  $F$ -displacements curves. The safety factor increased with  $z_B$ , being in the range of 1.96–2.19 and of 1.83–2.12 for the real and the artificial accelerograms, respectively (Table 7). The maximum reduction of  $F$  with respect to the static condition ( $F = 2.33$ ) was of about 21.5%, and occurred using the artificial accelerogram at  $z_B = 25$  m as input motion. For each of the assumed bedrock depths and for both artificial and real input motions, the computed failure mechanisms occurred in the downstream slope of the dam, involving its upper third.

Through the FE dynamic analyses some insight was gained on the seismic behaviour of the dam. Specifically, the computed

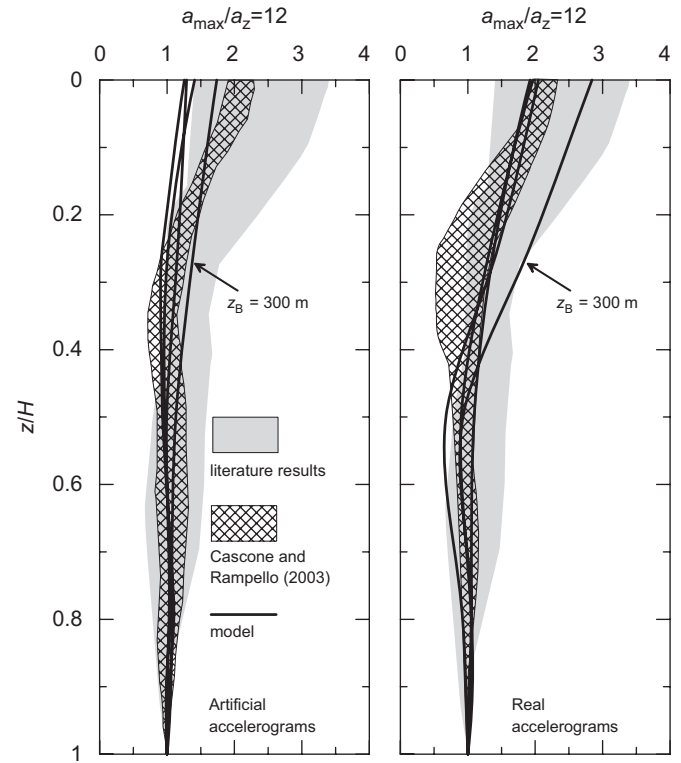


Fig. 22. Comparison between computed maximum acceleration profiles and published results.

Table 7  
Post-seismic stability evaluation

$z_B$	Artificial	Real
25	1.83	1.96
50	1.91	1.97
100	2.01	2.11
300	2.12	2.19

deviatoric strain was generally smaller than 0.8%, with the exception of confined zones located at the upstream toe of the dam; horizontal and vertical displacements through the dam were smaller than the values at the crest; at several instants during the earthquake, available shear strength was mobilised in a confined zone located in the upper third of the dam.

Comparison between the effective stress FE analyses and the displacement-based methods was carried out in terms of vertical displacements computed at the crest of the dam. Coupled effective stress dynamic analyses provided values of vertical displacements of 22–30 cm and of 8–16 cm using the artificial and real accelerograms as input motions, respectively. Using the accelerograms obtained from the 2D ground response analysis, the sliding block analysis yielded dam displacements of 10–40 cm, the higher values being in a fair agreement with effective stress FE analysis results.

For any of the seismic scenarios considered in this study and for each of the methods of analysis adopted, the estimated seismic performance of the dam was deemed satisfactory in that the maximum crest displacement was considerably lower than the service freeboard (2.6 m).

## References

- [1] Finn LWD, Ledbetter RH, Marcusson WF. North American practise for evaluating the seismic safety of embankment dams. In: Ishihara K, editor. *Earthquake Geotechnical Engineering*. Rotterdam: Balkema; 1997. p. 1227–52.
- [2] Finn LWD. State-of-the-art of geotechnical earthquake engineering practice. *Soil Dyn Earthquake Eng* 2000;20:1–15.
- [3] Finn LWD, Yogendrakumar M, Yoshida N, Yoshida H. TARA-3: a program to compute the response of 2-D embankments and soil-structure systems to seismic loadings. Canada: Department of Civil Engineering, University of British Columbia; 1986.
- [4] Griffiths DV, Prevost JH. Two- and three dimensional dynamic finite element analyses of the long valley dam. *Géotechnique* 1988;38:367–88.
- [5] Elgamal A-WM. Three dimensional seismic analysis of La Villita Dam. *J Geotech Eng ASCE* 1992;118:1937–58.
- [6] Seed HB, Seed RB, Lai SS, Khamenehpour B. Seismic design of concrete faced rockfill dams. In: *Concrete face rockfill dams—design, construction and performance*. ASCE; 1985. p. 459–78.
- [7] Gazetas G, Dakoulas P. Seismic analysis and design of rockfill dams: state-of-the-art. *Soil Dyn Earthquake Eng* 1992;11:27–61.
- [8] Özkan MY, Erdik M, Tunçer MA, Yılmaz Ç. An evaluation of Sürgü Dam response during 5 May 1986 earthquake. *Soil Dyn Earthquake Eng* 1996;15:1–10.
- [9] Troncoso JH, Krause AJ, Corser PG. Seismic design of lined face earth dams. In: *Proceedings of the second international conference on earthquake geotechnical engineering*, Lisbon; 1999. p. 703–9.
- [10] Cascone E, Rampello S. Decoupled seismic analysis of an earth dam. *Soil Dyn Earthquake Eng* 2003;23:349–65.
- [11] Whitman RW, Liao S. Seismic design of retaining walls. In: *Proceeding of the eighth world conference on earthquake engineering*, San Francisco; 1984. p. 533–40.
- [12] Ambraseys NA, Menu JM. Earthquake-induced ground displacements. *Earthquake Eng Struct Dyn* 1988;16:985–1006.
- [13] Jibson RW. Predicting earthquake-induced landslide displacements using Newmark's sliding block analysis. *Transportation Research Record* 1411, Transportation Research Board, National Research Council, Washington DC; 1993. p. 9–17.
- [14] Calabresi G, Rampello S, Sciotti A, Amorosi A. Diga sulla Marana Capacciotti: Verifica delle condizioni di stabilità e analisi del comportamento in condizioni sismiche. *Res. Rep. Dip. di Ingegneria Strutturale e Geotecnica*, Università di Roma La Sapienza; 2000.
- [15] EN 1998-1 Eurocode No. 8: design of structures for earthquake resistance of structures, CEN European Committee for Standardisation; 2003.
- [16] CNR-GNDT. L'attività del GNDT nel triennio 1993–1995, a cura di A. Corsanego, E. Faccioli, C. Gavarini, P. Scandone, D. Slejko, M. Stucchi; 1996.
- [17] Newmark NM. Effect of earthquakes on dams and embankments. *Géotechnique* 1965;15(2):139–60.
- [18] Cai Z, Bathurst RJ. Deterministic sliding block methods for estimating seismic displacements of earth structures. *Soil Dyn Earthquake Eng* 1996;15:255–68.
- [19] Rathje EM, Bray JD. An examination of simplified earthquake-induced displacement procedures for earth structures. *Can Geotech J* 1999;36:72–87.
- [20] Rathje EM, Bray JD. Nonlinear coupled seismic sliding analysis of earth structures. *J Geotech Geoenviron Eng ASCE* 2000;120(11):1002–14.
- [21] Vermeer P, Brinkgreve RBJ, Plaxis V7, *Material models manual*. Rotterdam: Balkema; 1998.
- [22] Schanz T. Zur modellierung des mechanischen verhaltens von reibungsma-terialen. *Habilitation*, Stuttgart Universität; 1998.
- [23] Schanz T, Vermeer PA, Bonnier PG. Formulation and verification of the hardening-soil model. In: Brinkgreve RBJ, editor. *Beyond 2000 in computational geotechnics*. Rotterdam: Balkema; 1999. p. 281–90.
- [24] Viggiani G. Small strain stiffness of fine grained soils. PhD thesis, City University, London; 1992.
- [25] Rampello S, Viggiani GMB. Pre-failure deformation characteristics of geomaterials. Discussion leader report on session 1a: laboratory tests. In: *Proceedings of the second international symposium on 'pre-failure deformation characteristics of geomaterials'*, vol. 2, Torino; 2001. p. 1279–89.
- [26] Lysmer J, Kuhlemeyer RL. Finite dynamic model for infinite media. *J Eng Mech ASCE* 1969;95(4):859–77.
- [27] Kuhlemeyer RL, Lysmer J. Finite element method accuracy for wave propagation problems. *J Soil Mech Found ASCE* 1973;99(5):421–7.
- [28] Poulos HG, Booker JR, Ring GJ. Simplified calculation of embankment deformations. *Soils Found* 1972;12(4):1–17.
- [29] Pagano L, Desideri A, Vinale F. Interpreting settlement profiles of earth dams. *J Geotech Geoenviron Eng ASCE* 1998;124(10):923–32.
- [30] Gazetas G. Shear vibration of vertically inhomogeneous earth dams. *Int J Numer Anal Methods Geomech* 1982;6:219–41.
- [31] Makdisi FI, Kagawa T, Seed HB. Seismic response of earth dams in triangular canyons. *J Geotech Eng ASCE* 1982;108(10):1328–37.
- [32] Prato CA, Delmastro E. 1-D seismic analysis of embankment dams. *J Geotech Eng ASCE* 1987;113(8):904–9.
- [33] Gazetas G. Seismic response of earth dams: some recent developments. *Soil Dyn Earthquake Eng* 1987;6:2–47.
- [34] Abouseeda H, Dakoulas P. Non-linear dynamic earth dam-foundation interaction using a BE-FE method. *Earthquake Eng Struct Dyn* 1998;27:917–36.